**Figure S1. Schematic of epithelial marker apical intensity calculations. Related to Figure 1, Figure 2, Figure 5 and Figure 6.**

(A) Transverse sections of stage 28 control embryo stained for tropomyosin (red) and ZO-1 (green). To calculate apical intensity, the red and green channels are first split. The tropomyosin channel is used to segment out and create a mask for cardiomyocytes. The ZO-1 channel has intensity normalized to background signal in the endoderm and undergoes a small Gaussian blur (kernel = 2 pixels). (B) Applying the mask to the normalized ZO-1 channel generates an image with only ZO-1 expression in cardiomyocytes. A 10-pixel wide linear region around along the apical surface is created to measure apical intensity. Scale bar = 50 µm. (C) 3D projection of the ventral, cardiomyocyte-masked, ZO-1 expression, showing apical intensity measurements at 4 different z-locations.
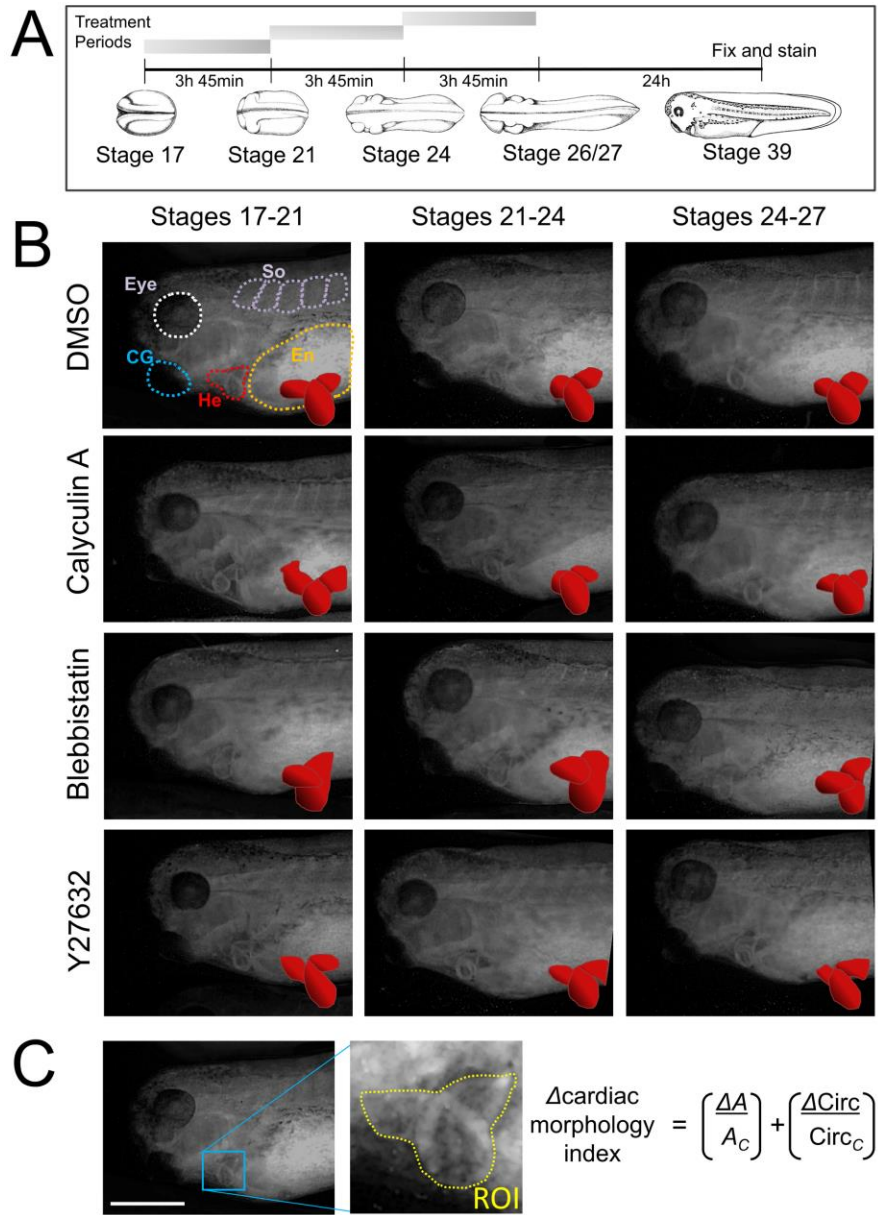
**Figure S2. Acute small molecule inhibitor treatments reveal stage-specific requirements of actomyosin contractility for proper heart development. Related to Figure 2I.**

(A) Schematic of different treatment periods and how they relate to embryonic development. Drawings after [S1]. (B) Stage 39 embryos exposed to acute stage-specific small molecule inhibitor treatments. Shape of heart drawn and expanded for emphasis (red). (C) The Δcardiac morphology index is calculated from the morphology of a hand-drawn region of interest (yellow dashed line; ROI) surrounding the larval heart (calculated values in Figure 2I). In addition to the heart (He) other features of the tadpole are visible including somites (So), cement gland (CG), and endoderm (En). Cardiac morphology (Δcardiac morphology index) is calculated from the difference of the heart area from mean (ΔA), average control heart area ($A_c$), difference of circularity of the ROI from the mean (ΔCirc), and average control heart circularity ($Circ_c$). Scale bar = 500 μm.
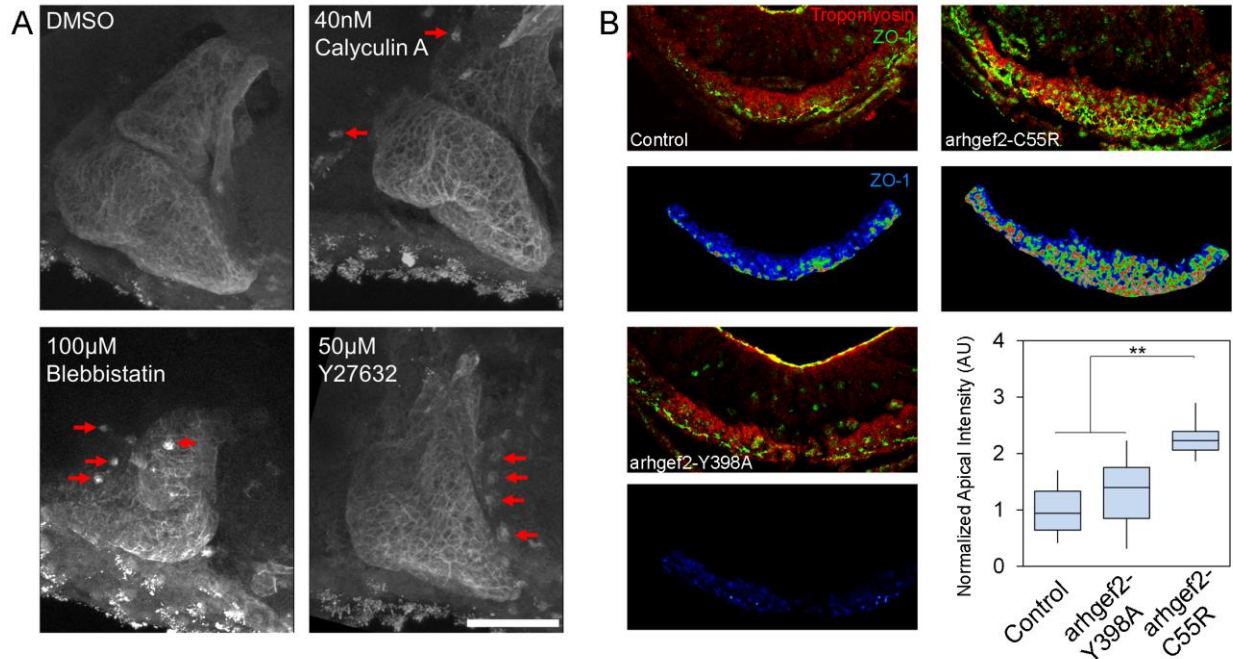
**Figure S3. Chronic small molecule inhibitor treatment results in failure of cardiomyocytes to incorporate into vertebrate heart while targeted injections to perturb endoderm contractility with arhgef2 enhances ZO-1 polarity. Related to Figure 2 and Figure 5.**

(A) 3D projections of Stage 39 embryonic hearts following chronic small molecule inhibitor treatment (stages 20 to 28, ~11 hours) stained for tropomyosin. Arrows show tropomyosin positive cells in the ventral heart forming region that do not assemble into the developing heart. Scale bar = 100 μm. (B) Transverse sections of stage 28 embryos stained for tropomyosin (red) and ZO-1 (green) with ZO-1 intensities masked by tropomyosin expression (pseudo-color). Embryos with endoderm injected with arhgef2-C55R show elevated ZO-1 expression relative to the rhodamine dextran (RDA) injected control and embryos injected with arhgef2-Y398A. Normalized intensities of arhgef2-C55R injected embryos are significantly higher than either RDA injected controls of arhgef2-Y398 injected embryos. Scale bar = 50 μm. ** denotes p < 0.01.
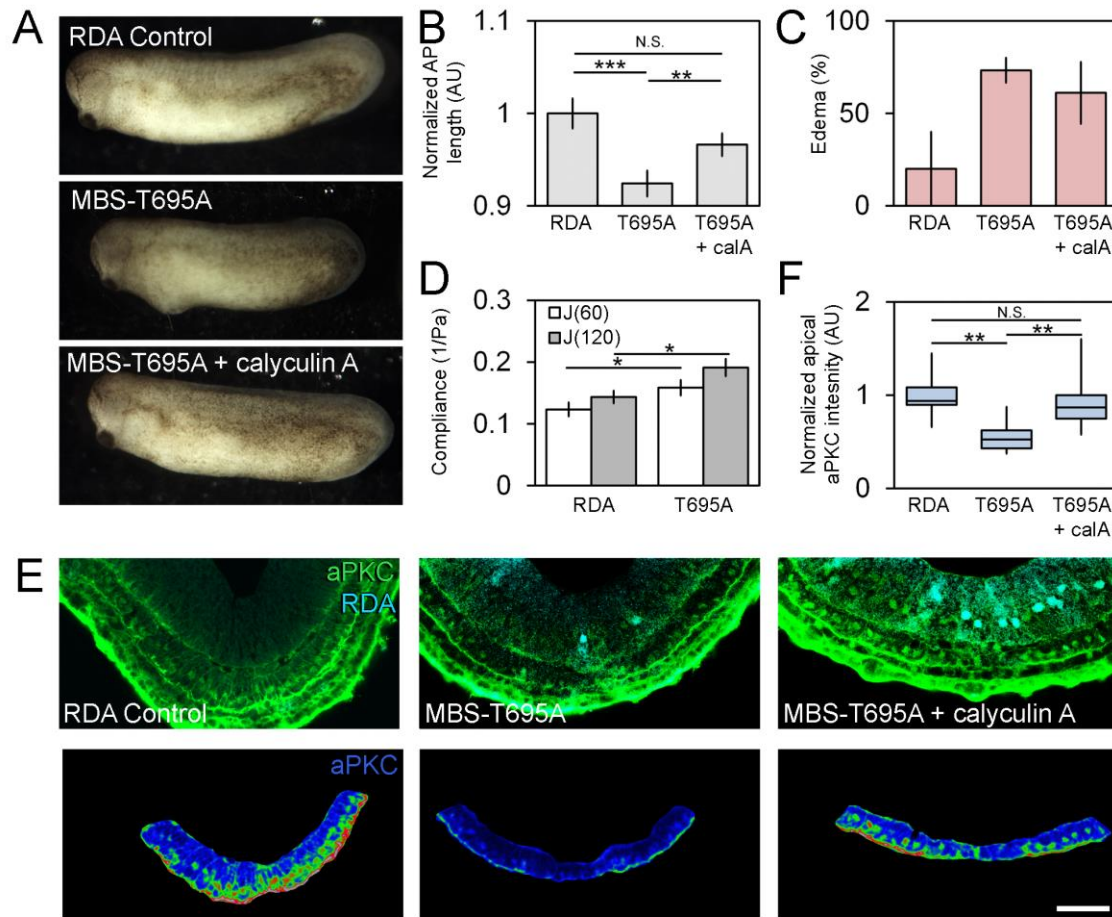
**Figure S4. Targeted injections to perturb endoderm contractility with MBS-T695A increases compliance and reduces aPKC localization. Related to Figure 5.**

(A) Tadpoles injected with either rhodamine dextran (RDA) or a constitutively active MBS-T695A. (B) MBS-T695A injected embryos exhibit reduced anterioposterior length (N= 14-19 embryos over two clutches) and (C) have higher rates of edema presentation per clutch (N = 2 clutches). These defects can be partially rescues by treatment with calyculin A during Stages 20-28. (D) Embryos expressing MBS-T695A in their anterior endoderm have increased compliance in the HFR (N = 13-14 embryos over two clutches). (E) Top panels show immunofluorescent staining of Stage 28 embryos with aPKC (green) and fixed injected RDA (cyan). Bottom panel shows manually segmented HPCs with aPKC in pseudocolor LUT. (F) Normalized apical intensity measurements of aPKC shows reduced intensity in HPCs with MBS-T695A injected into endoderm, which can be rescued with calyculin A treatment (N = 6-8 embryos over two clutches). Scale bar = 50 μm. Error bars represent mean ± SEM. * denotes p < 0.05; ** denotes p < 0.01; *** denotes p < 0.001.
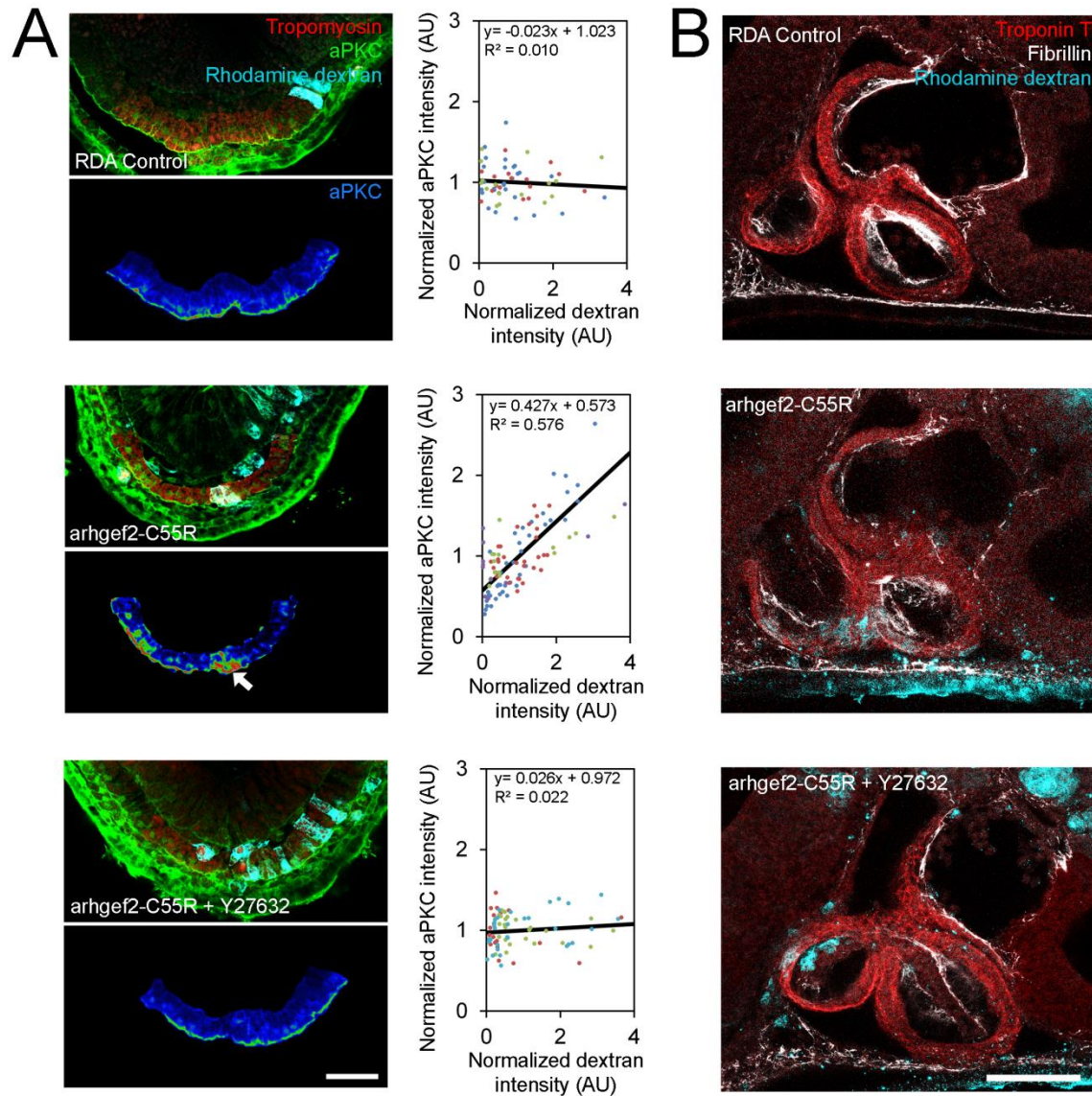
**Figure S5. Targeted injections to perturb HPC contractility shows cell-autonomous mechanics influence MET. Related to Figure 5.**

(A) Transverse sections of stage 28 embryos stained for tropomyosin (red) and ZO-1 (green) with rhodamine dextran (RDA; cyan) showing expression of construct target injected into HPCs. Expression of arhgef2-C55R results in visibly elevated expression of aPKC (arrow). Quantification of individual cell apical intensities of RDA and aPKC show significantly correlation in arhgef2-C55R expressing HPCs but not RDA controls or embryos expressing arhgef2-C55R and treated with 50μM Y27632. Scale bar is 50 μm. (B) Stage 39 embryos with HPC-targeted expression of injected constructs. arhgef2-C55R embryos show relatively normal hearts with defects localized to where arhgef2-C55R is expressed. Treatment with Y27632 partially rescues these defects. Scale bar = 100 μm.
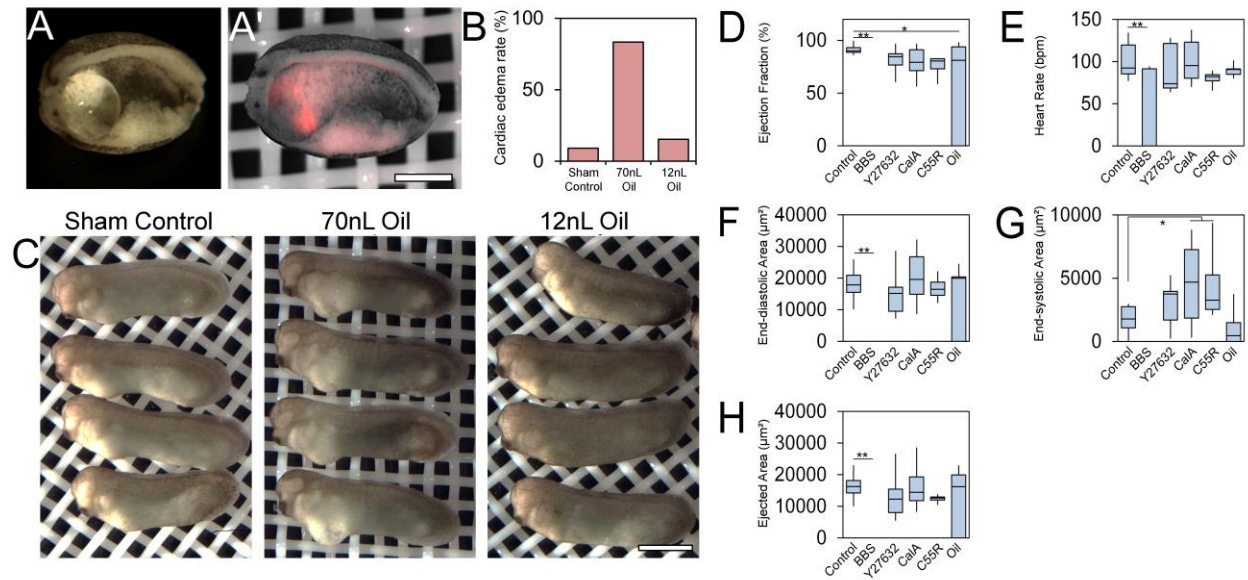
**Figure S6. Cardiac defects resulting from mineral oil injects are caused by stress on the anterior ventral tissues and graph representations of hemoglobin contrast subtraction angiography data. Related to Figures 6 and 7.**

(A) Embryo fixed and sectioned one hour after injection with mineral oil (~70nL) shows oil remains localized to the anterior portion of the embryo. (A') DiI dye transfer from mineral oil to cells shows anterior ventral endoderm tissues are in direct contact with the stress-inducing oil. Scale bar = 500 µm. (B) Edema rates show elevated cardiac defects in full amount mineral oil (~70nL) injected embryos but not sham controls or reduced amount oil (~12nL). (C) Embryos were either wounded with the microinjection needle (sham control), injected with the full amount of mineral oil (~70nL) or injected with one-sixth of the full amount of mineral oil (~12 nL), which did not cause expansion of ventral tissues. Scale bar = 1 mm. Boxplots shown for (D) ejection fraction, (E) heart rate, (F) end-diastolic volume, (G) end-systolic volume and (H) ejected volume. * denotes $p < 0.05$; ** denotes $p < 0.01$.
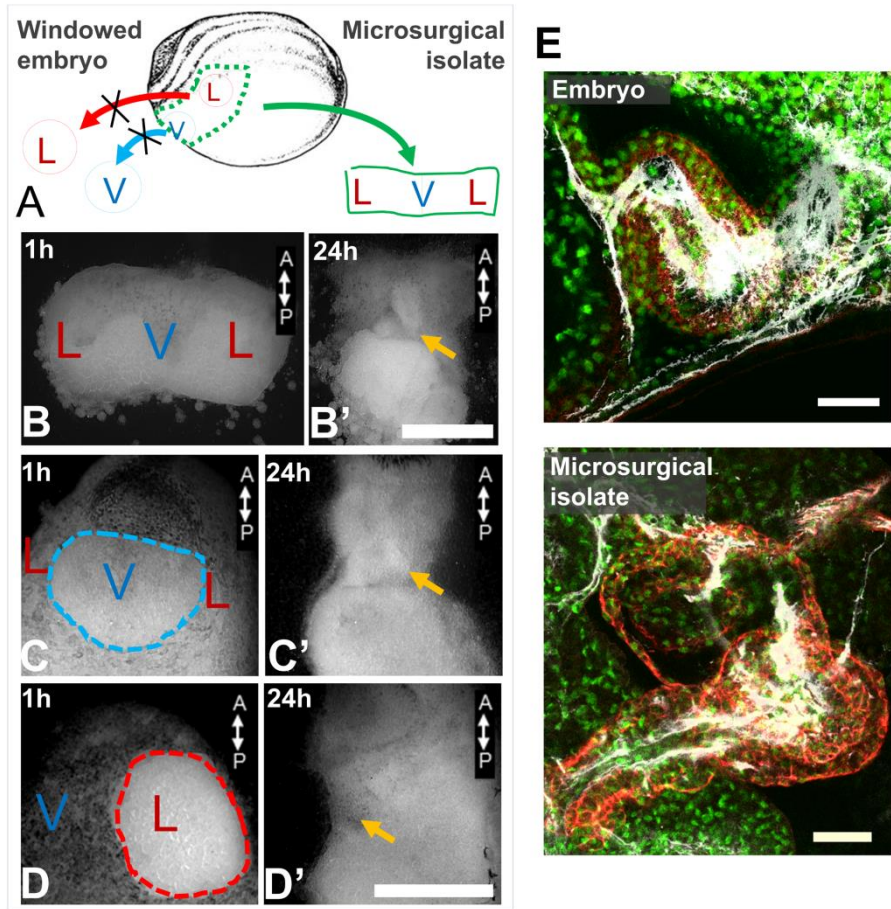
**Figure S7. Microsurgical manipulations to visualize HPCs in *Xenopus*. Related to Experimental Procedures.**

(A) Schematic of microsurgical manipulations to visualize HPC migration. (B) Microsurgical isolates at 1 h and 24 h. (C) Ventral windowed embryo at 1 h and 24 h. (D) Lateral windowed embryo at 1 h and 24 h. Yellow arrows mark location of beating heart. Scale bar = 500 µm. (E) Stage 33 embryo and equivalent stage microsurgical isolate stained for troponin T (red), fibrillin (white) and nuclei (green). Scale bar = 50 µm.

## Supplemental Experimental Procedures

### Xenopus embryos, microsurgery and microinjections

*Xenopus laevis* embryos were obtained via standard methods [S2] and cultured in 1/3× modified Barth Solution (MBS; [S3])). Both intact embryos and tissue explants can be used to expose development of heart progenitors for high resolution imaging (Figure S7A). *Ex vivo* tissue isolates consisting of the ventral mesoderm and the bilateral fields of anterior lateral plate mesoderm are microsurgically removed from the embryo (Figure S7B) and cultured in Danilchik's For Amy (DFA; [S4] media supplemented with antibiotic and antimycotic (Sigma). Amphibian *ex vivo* tissue isolates have a long history in exposing fundamental principles of developmental biology. Amphibian tissue isolates have been and continue to be a cornerstone of reductionist methods used to expose critical signaling pathways and routes of cell-cell communication. Without these methods it would have been extremely challenging to isolate specific pathways and principles of signal transduction, cell adhesion, and morphogenesis. Tissue isolates are useful in biomechanical studies for the same reason they are useful for biochemical studies. Firstly, tissue isolates are composed of thousands of cells that retain key cell-cell communication pathways, cell-cell and cell-ECM adhesions, and large scale microanatomy found in the intact embryo. We have confirmed that post-gastrulation stage tissue isolates are fully capable of engaging programs of morphogenesis and generating structures that are indistinguishable from those structures produced in vivo and we expect both biochemical and biomechanical processes continue to operate as they would in vivo. Our specific application of tissue isolates of the heart forming region is based on classical applications of microsurgical methods to identify patterning factors operating in gastrula stage embryos [S5, S6]. Our assumption that mechanical conditions in isolates approximates those in vivo are based on our work on the material properties and forces generated within tissue isolates over a series of biomechanical studies we have conducted both in vivo [S7-S10] and with ex vivo tissues [S11-S15].

In addition to *ex vivo* isolates, intravital "windowed" embryos can be generated by microsurgically removing the ventral ectoderm (Figure S7C). mRNA encoding fluorescent protein constructs were injected at the one- or two-cell stage to visualize nuclei (H2B-mCherry), plasma membrane (CAAX-GFP) or F-actin (moesin-GFP) . Targeted injections of mRNA to endoderm or HPCs were carried out at the 32-cell stage based on established *Xenopus* fate mapping protocols [S16, S17]. mRNA encoding arhgef2-C55R or MBS-T695A was co-injected with rhodamine dextran amine (RDA) for visualization purposes. Accuracy of targeted injections was verified visually by RDA prior to fixing embryos at Stage 28.

### Small-molecule inhibitor treatments

In order to manipulate tissue stiffness through cell contractility, embryos were either subjected to a chronic (from Stage 20 to 28) or acute (Figure S2A) treatment with Y27632 (50 µM) [S18], Blebbistatin (100 µM) [S19], or Calyculin A (50 nM) [S20].

### Histology, immunostaining and confocal microscopy

Tissue isolates or whole embryos were fixed with either 4% paraformaldehyde for 2 hours or Dents fixative overnight. Posterior halves of embryos were removed prior to staining to minimize antibodies getting stuck in gut cavity. After blocking, immunofluorescence staining was carried out with primary antibodies JB3, CT3, CH1 (Developmental Studies Hybridoma Bank), aPKC (Santa Cruz), ZO-1 (Invitrogen), 4H2 (courtesy of Douglas DeSimone), β-catenin (Sigma-Aldrich). Appropriate secondaries (1:1000; Jackson ImmunoResearch) were then used to stain overnight. Nuclei were identified with YO-PRO-1 (ThermoFisher). Transverse sections of embryos were generated either using a vibratome or manually using a scalpel and then dehydrated and cleared. Confocal stacks were collected using a laser-scanhead mounted on an inverted compound microscope (Leica SP5). For quantification purposes, acquisition parameters were kept constant throughout experiments and slices in stacks were collected at 1 µm z-intervals. To quantify apical intensity of epithelial markers, stacks were masked using the tropomyosin channel to ensure only cardiomyocytes were considered, normalized to the background fluorescence in the endoderm cells, summed over consecutive 5 µm z-volumes and then blurred using a small kernel Gaussian blur (Figure S1A). Intensity along a 10-pixel thick linear region (Figure S1B) along the apical surface was measured and

measurements were done at 4 z-depths for each embryo (Figure S1C). For the acute small-molecule inhibitor treatment studies (Figure 2I and Figure S2), fluorescence images were acquired with CCD camera (QImaging) mounted on a fluorescence-equipped stereomicroscope (Olympus). Images were then double-blinded for ROI drawing around the tadpole heart. The cardiac morphology index was calculated in order to consider both heart size and shape, using the area and circularity obtained from the drawn ROI (Figure S2C).

*Compliance measurements using micro-aspiration*

To measure the mechanical properties of the heart forming region, embryos were placed in the high-pressure reservoir of a dual-reservoir micro-aspirator apparatus (Figure 2D, [S9, S21, S22]). Embryos were gently compressed using hair tools such that the ventral heart forming region (just medial of the ventral midline) was up against a 125 μm diameter channel cast across a PDMS block to form a seal across the opening of the channel. A pressure differential at the channel opening was controlled hydrostatically using a computer-controlled syringe pump. After calibrating the channel to obtain zero flow, a small baseline pressure of approximately -1.5 Pa was applied in order to initiate suction and seal the embryo onto the channel opening. To permit tissue relaxation prior to testing, we allowed a 5 minute pause before the 155-second micro-aspiration protocol was initiated. At the start of the protocol, the embryo was imaged at 1 frame per second to obtain an initial aspiration length for the tissue. After 5 frames, the syringe pump removed 800 μL of media from the low-pressure reservoir resulting in a final -10.1 Pa suction pressure applied to the aggregate. After 120 seconds, 800 μL was media was replaced to return to the baseline pressure. Imaging continued for an additional 30 seconds to confirm the embryo was properly sealed onto the channel opening. If carrying out repeated measurements on the same sample, the embryo was rotated to a different position. The tissue boundary in the microchannel was tracked either manually or automatically with Canny-Deriche edge detection [S23]. The aspirated length was measured and the data was fit to the power-law model for creep compliance, which has previously been shown to provide an adequate fit for embryonic tissue responses to stress-application [S9]. Time-dependent compliance at 60 seconds (fast response) and 120 seconds (steady-state) is reported as the measurement of embryo mechanical properties. Compliance calculations for each sample are independent of the magnitude of the pressure applied [S9]. The suction force of -10.1 Pa was chosen in order to sufficiently displace aggregate tissues within the resolution of our imaging system without exceeding the critical pressure ($P_c$), thus ensuring measurements are representative of viscoelastic properties [S24]. Choice of a low pressure ($P < P_c$; [S9]) for microaspiration reports the bulk, or composite tissue, compliance of a 125 μm diameter patch to reflect the contribution of all three germ layers in the HFR (Figure 2D). These low suction pressures generate a small strain that mimics the physiological strain observed during development of the HFR. To calculate the stress index in Figure 4F, strain rate values were taken from the data in Figure 4D at the developmental stages corresponding to the compliance measurements in Figure 4E: 19 (2h), 21 (4h) and 23 (6h). Compliance values were inverted to obtain equivalent modulus and then multiplied by the strain rate to calculate a stress index.

Our reported compliance values indicate *Xenopus* ventral tissue to be extremely soft, within a range of 1-10 Pa, which is on par with other amphibian embryos [S7-S9, S12-S14, S25-S28]. To explore the universal role of mechanotransduction during MET will require comparative analyses of the mechanical conditions that prevail during METs across different species, tissues, and stages. The absolute mechanical properties of embryonic tissues appear specific for each organism, tissue and age. For instance, the mechanical properties of gastrulating *Xenopus* and sea urchin embryos can differ by a 1000-fold [S29], avian HPCs at the early tube stage are stiffer [S30], and later stages of the developing mouse heart are stiffer still [S31]. Still, the developmental profiles of different species share common trends [S32]; embryos stiffen as they age [S33] and mechanical properties can vary as much as two-fold between siblings [S21].

*Ventral tissue elongation calculations*

For visualization of ventral elongation (Figure 4A-D), the dorsal side of Stage 14 *Xenopus* embryos were wounded and placed onto a fibronectin coated dish, to allow the dorsal tissues to adhere and stabilize the embryo. Time lapse images were captured using a CCD camera (Scion Corp, Frederick, MA) mounted onto a stereomicroscope using Micro-Manager [S34]. Time lapses of ventral elongation were input a finite element registration based algorithm, using open source libraries of ITK [S35], which was described previously [S36]. A grid of points was manually chosen and consecutive frames were registered, to calculate a displacement map to map one frame onto the next. The

calculated displacements were then applied to the grid points and then overlaid onto the image. Since HPCs are located within 50 µm of the ventral ectoderm surface of the embryo, and ectoderm and mesoderm appear mechanically coupled at these stages, our analysis assumes that deformation of HPCs and the HFR could be approximated by deformations observed in ventral ectoderm.

### Low-resolution traction force microscopy

*Ex vivo* ventral tissue isolates expressing a membrane-targeted GFP (CAAX-GFP) were cultured on a 0.05% polyacrylamide gel conjugated with human fibronectin (Sigma) containing red and far red beads (Molecular Probes) following an established protocols [S14, S37]. Tissue isolates were allowed to adhere to the gel and develop for 2 hours prior to imaging. Live imaging of cell movement and bead displacement was done on a laser-scanning confocal microscope (Leica SP5, Leica Microsystems). At the conclusion of the experiment, tissue isolates were exposed to Trypsin to induce cell release from the gel, in order to obtain a zero force image of the gel. Customized implementation of rigid registration algorithms from the Insight Toolkit (ITK; [S35]) was used to register the time-lapse sequences of the cell and each individual bead channel to the zero force image, using a portion of the gel without cells over top as a landmark for registration. Bead and cell displacements were calculated using a finite element registration algorithm from ITK, registering each consecutive frame to the zero force images. Displacements in the two separate bead channels were averaged together to improve accuracy [S38]. Bead displacements and cell displacements were averaged over 30 minute increments, in order to remove oscillations from individual cell protrusion and release cycles. Cosine similarity scores were calculated using a custom macro written in ImageJ [S23].

### Long-term time-lapse nuclei tracking

Nkx2.5-GFP transgenic embryos were injected with a Histone-2B-mCherry mRNA. Using the intravital ventral "windowed" embryo model, we image mesoderm development over 24 hours until the GFP signal was detectable to allow for positive identification of HPCs. Using the nkx2.5-GFP intensity to create a mask for the last frame of the time-lapse sequence, nuclei were tracked retroactively using a combination of watershed segmentation and finite element registration image filters from ITK. In brief, nuclei were segmented out and consecutive frames were registered to calculate predictive nuclei displacement values. Those predictive displacements were applied to a nucleus centroid and then nuclei in the next frame were matched based on minimum distance from that predictive value. Information on unmatched nuclei was saved to retry matching for up to the next 6 frames (1 hour). Persistence was calculated over thirty minutes as the effective distance traveled over the total distance. Collectiveness is defined as the cosine similarity between motion vectors of a given nuclei and all of the other nuclei within its "neighborhood", defined as within a 40 µm radius. Average values of parameters were calculated for each nucleus over the time periods defined in Fig 3H.

### Mineral oil injections

Stage 21 embryos were injected with approximately 70 nL of mineral oil until expansion of ventral tissues was visible. Embryos fixed 1 hour after oil injection show that the oil mainly stays in the anterior portion of the embryo (Figure S6A). Fluorescence transfer of DiI dissolved in the mineral oil further confirms that the oil seemed to remain in the anterior portion of the archenteron (Figure S6A'), where it would exert the most force on the ventral heart forming region. Accuracy of target was confirmed visually using fluorescence of DiI (red in Figure S6A'). After injection, embryos were cultured in 1/3x MBS until needed. Based on compliance measurements of the HFR at this stage (Figure 4E), we estimate 0.3 Pa of stress is applied to the HFR.

### Assessment of cardiac function

To assess the cardiac function of a larval heart, we adapted a protocol previously established [S39]. Briefly, embryos were cultured three days and embedded in 3% ultra-low melting point agarose. Time-lapse sequences of heartbeats were recorded 60 frames-per-second using a DSLR camera (Canon T3i) mounted onto the video port of a

fluorescence-equipped stereoscope (Olympus). A GFP filter was used to further enhance native hemoglobin contrast. Angiography was accomplished by applying custom image analysis macros to the RGB time-lapse sequences (ImageJ; [S23]). RGB videos were separated into red and green channels. Red channels were multiplied by a constant to achieve the same mean intensity as the green channel. The green channel was subtracted from the red channel producing a time-lapse sequence of hemoglobin contrast subtraction angiography images (HCSA) which were auto-thresholded to highlight relative changes in hemoglobin (hemoglobin blush). Quantitative time-series analysis of hemoglobin blush generated standard echocardiograph-like parameters of cardiac function [S39] that were averaged over at least 15 cardiac cycles for each embryo.

*Statistical analysis*

For each experiment, an ANOVA was first done to determine if the clutch-to-clutch variation was significant to confirm that data from multiple clutches could be pooled. An ANOVA was then performed on pooled data, with a planned simple contrast to compare the appropriate control to each treatment. Correlations for traction co-alignment over time (Figure 3D), dextran-aPKC colocalization (Figure S5A) and normalized apical intensity over time and compliance (Figure 7E-F) was estimated by fitness of a simple linear regression. Statistical analyses were performed using IBM SPSS Statistics 22. Graphs were produced with Microsoft Excel, with information about sample size and the error bars located in each figure legend.

### *Supplemental References*

S1.  Nieuwkoop, P.D., and Faber, J. (1967). Normal tables of *Xenopus laevis* (Daudin). (Amsterdam: Elsevier North-Holland Biomedical Press).
S2.  Kay, B.K., and Peng, H.B. (1991). *Xenopus laevis*: practical uses in cell and molecular biology., Volume 36, (New York: Academic Press).
S3.  Sive, H.L., Grainger, R.M., and Harland, R.M. (2000). Early development of Xenopus laevis: a laboratory manual, (Cold Spring Harbor, New York: Cold Spring Harbor Laboratory Press).
S4.  Sater, A.K., Steinhardt, R.A., and Keller, R. (1993). Induction of neuronal differentiation by planar signals in Xenopus embryos. Dev Dyn *197*, 268-280.
S5.  Nascone, N., and Mercola, M. (1995). An inductive role for the endoderm in Xenopus cardiogenesis. Development *121*, 515-523.
S6.  Schneider, V.A., and Mercola, M. (1999). Spatially distinct head and heart inducers within the Xenopus organizer region. Curr Biol *9*, 800-809.
S7.  von Dassow, M., and Davidson, L.A. (2009). Natural variation in embryo mechanics: gastrulation in Xenopus laevis is highly robust to variation in tissue stiffness. Dev Dyn *238*, 2-18.
S8.  von Dassow, M., Miller, C.J., and Davidson, L.A. (2014). Biomechanics and the thermotolerance of development. PLoS One *9*, e95670.
S9.  von Dassow, M., Strother, J.A., and Davidson, L.A. (2010). Surprisingly simple mechanical behavior of a complex embryonic tissue. PLoS One *5*, e15359.
S10. Feroze, R., Shawky, J.H., von Dassow, M., and Davidson, L.A. (2015). Mechanics of blastopore closure during amphibian gastrulation. Dev Biol *398*, 57-67.
S11. Moore, S.W. (1994). A fiber optic system for measuring dynamic mechanical properties of embryonic tissues. IEEE Transaction on Biomedical Engineering *41*, 45-50.
S12. Moore, S.W., Keller, R.E., and Koehl, M.A.R. (1995). The dorsal involuting marginal zone stiffens anisotropically during its convergent extension in the gastrula of *Xenopus leavis*. Development *121*, 3130-3140.
S13. Zhou, J., Kim, H.Y., and Davidson, L.A. (2009). Actomyosin stiffens the vertebrate embryo during critical stages of elongation and neural tube closure. Development *136*, 677-688.
S14. Zhou, J., Kim, H.Y., Wang, J.H.-C., and Davidson, L.A. (2010). Macroscopic stiffening of embryonic tissues via microtubules, Rho-GEF, and assembly of contractile bundles of actomyosin. Development *137*, 2785-2794.

S15.    Zhou, J., Pal, S., Maiti, S., and Davidson, L.A. (2015). Force production and mechanical adaptation during convergent extension. Development *142*, 692-701.

S16.    Dale, L., and Slack, J.M. (1987). Fate map for the 32-cell stage of Xenopus laevis. Development (Cambridge, England) *99*, 527-551.

S17.    Bauer, D.V., Huang, S., and Moody, S.A. (1994). The cleavage stage origin of Spemann's Organizer: analysis of the movements of blastomere clones before and during gastrulation in Xenopus. Development *120*, 1179-1189.

S18.    Ishizaki, T., Uehata, M., Tamechika, I., Keel, J., Nonomura, K., Maekawa, M., and Narumiya, S. (2000). Pharmacological properties of Y-27632, a specific inhibitor of rho-associated kinases. Mol Pharmacol *57*, 976-983.

S19.    Straight, A.F., Cheung, A., Limouze, J., Chen, I., Westwood, N.J., Sellers, J.R., and Mitchison, T.J. (2003). Dissecting temporal and spatial control of cytokinesis with a myosin II Inhibitor. Science *299*, 1743-1747.

S20.    Ishihara, H., Martin, B.L., Brautigan, D.L., Karaki, H., Ozaki, H., Kato, Y., Fusetani, N., Watabe, S., Hashimoto, K., Uemura, D., et al. (1989). Calyculin A and okadaic acid: inhibitors of protein phosphatase activity. Biochem Biophys Res Commun *159*, 871-877.

S21.    von Dassow, M., and Davidson, L.A. (2009). Natural variation in embryo mechanics: gastrulation in Xenopus laevis is highly robust to variation in tissue stiffness. Dev Dyn *238*, 2-18.

S22.    Kim, H.Y., Jackson, T.R., Stuckenholz, C., and Davidson, L.A. (submitted). Tissue mechanics drives mesenchymal-to-epithelial transition in embryonic cell aggregates.

S23.    Schneider, C.A., Rasband, W.S., and Eliceiri, K.W. (2012). NIH Image to ImageJ: 25 years of image analysis. Nat methods *9*, 671-675.

S24.    Sato, M., Levesque, M.J., and Nerem, R.M. (1987). An application of the micropipette technique to the measurement of the mechanical properties of cultured bovine aortic endothelial cells. Journal of biomechanical engineering *109(1)*, 27-34.

S25.    Benko, R., and Brodland, G.W. (2007). Measurement of in vivo stress resultants in neurulation-stage amphibian embryos. Ann Biomed Eng *35*, 672-681.

S26.    Wiebe, C., and Brodland, G.W. (2005). Tensile properties of embryonic epithelia measured using a novel instrument. J Biomech *38*, 2087-2094.

S27.    Kalantarian, A., Ninomiya, H., Saad, S.M., David, R., Winklbauer, R., and Neumann, A.W. (2009). Axisymmetric drop shape analysis for estimating the surface tension of cell aggregates by centrifugation. Biophys J *96*, 1606-1616.

S28.    Luu, O., David, R., Ninomiya, H., and Winklbauer, R. (2011). Large-scale mechanical properties of Xenopus embryonic epithelium. Proc Natl Acad Sci U S A *108*, 4000-4005.

S29.    Davidson, L.A., Oster, G.F., Keller, R.E., and Koehl, M.A. (1999). Measurements of mechanical properties of the blastula wall reveal which hypothesized mechanisms of primary invagination are physically plausible in the sea urchin Strongylocentrotus purpuratus. Dev Biol *209*, 221-238.

S30.    Shi, Y., Varner, V.D., and Taber, L.A. (2015). Why is cytoskeletal contraction required for cardiac fusion before but not after looping begins? Phys Biol *12*, 016012.

S31.    Majkut, S., Dingal, P.C., and Discher, D.E. (2014). Stress sensitivity and mechanotransduction during heart development. Curr Biol *24*, R495-501.

S32.    Zamir, E.A., and Taber, L.A. (2004). Material properties and residual stress in the stage 12 chick heart during cardiac looping. J Biomech Eng *126*, 823-830.

S33.    Zhou, J., Kim, H.Y., and Davidson, L.a. (2009). Actomyosin stiffens the vertebrate embryo during crucial stages of elongation and neural tube closure. Development (Cambridge, England) *136*, 677-688.

S34.    Edelstein, A.D., Tsuchida, M.A., Amodaj, N., Pinkard, H., Vale, R.D., and Stuurman, N. (2014). Advanced methods of microscope control using muManager software. J Biol Methods *1*.

S35.    Yoo, T.S., Ackerman, M.J., Lorensen, W.E., Schroeder, W., Chalana, V., Aylward, S., Metaxas, D., and Whitaker, R. (2002). Engineering and algorithm design for an image processing Api: a technical report on ITK--the Insight Toolkit. Stud Health Technol Inform *85*, 586-592.

S36.    Kim, Y., Hazar, M., Vijayraghavan, D.S., Song, J., Jackson, T.R., Joshi, S.D., Messner, W.C., Davidson, L.A., and LeDuc, P.R. (2014). Mechanochemical actuators of embryonic epithelial contractility. Proc Natl Acad Sci U S A *111*, 14366-14371.

S37.    Leach, J.B., Brown, X.Q., Jacot, J.G., Dimilla, P.A., and Wong, J.Y. (2007). Neurite outgrowth and branching of PC12 cells on very soft substrates sharply decreases below a threshold of substrate rigidity. J Neural Eng *4*, 26-34.

S38.   Sabass, B., Gardel, M.L., Waterman, C.M., and Schwarz, U.S. (2008). High resolution traction force microscopy based on experimental and computational advances. Biophysical journal *94*, 207-220.

S39.   Deniz, E., Jonas, S., Khokha, M., and Choma, M.A. (2012). Endogenous contrast blood flow imaging in embryonic hearts using hemoglobin contrast subtraction angiography. Opt Lett *37*, 2979-2981.